Design of an Instrument to Measure Optical Reflectance of Scintillating Crystal Surfaces

Martin Janecek, *Member, IEEE*, and William W. Moses, *Fellow, IEEE*

Abstract—In order for a Monte Carlo simulation to be accurate in predicting and optimizing the light collection in scintillation detectors, the light reflectance off an internal surface within the scintillating crystal must be understood well. We present design studies for an instrument that will accurately measure the reflectance distribution within a scintillating crystal. A laser is aimed towards the center of a 50.8-mm diameter scintillating crystal hemisphere. The laser can be positioned at any arbitrary angle. The laser beam is reflected off the flat surface of the hemisphere and the light distribution is measured by a movable array of photodiodes that can measure the reflected light over the entire 2π solid angle. Thirty-six PIN photodiodes, mounted in two rows and offset to each other by half the length of a photodiode, measure the reflected light. The currents from the photodiodes are switched through a multiplexer to a digital multimeter, where the current is recorded. The current measurements give a dynamic range of 10^5:1. A LabVIEW program controls the motion of the laser and photodiodes, the switch, and the data collection. The mechanical set-up is placed inside of a light-tight glove box. By flowing dry nitrogen gas through the glove box we can control the water content in the atmosphere and so measure hydroscopic scintillators.

Index Terms—Lambertian reflection, light collection, Monte Carlo methods, scintillating crystals

I. INTRODUCTION

MONTE Carlo simulation is often used to predict and optimize the light collection from scintillation crystals [1-5]. To accurately predict and optimize the light collection, e.g. by using DETECT [6], [7] or Litrani [8] Monte Carlo software, the crystals surface characteristics have to be understood well. A small error in the angular light distribution multiplies through the numerous reflections within the crystal before the light exits the crystal and is detected, and the small error in the light reflectance distribution will thus accumulate a large error at the exit surface. However, the light reflectance inside of scintillating crystals are poorly understood, particularly for rough-cut or

chemically etched surfaces as well as for various attached reflector materials, and reflections are therefore generally assumed to be either purely specular or purely diffuse (Lambertian) [1-6].

In this paper we describe the design of an instrument that will measure the angular distribution of light reflection within a scintillating crystal. An error analysis is performed to estimate the accuracy of the proposed instrument, and the component selection, including the testing of all the essential components, is presented.

II. DESIGN

A. Concept

To be able to measure the reflectance distribution inside of a scintillator crystal, we need to: 1) be able to create a light beam *inside* of the scintillator that will strike the reflection surface at an arbitrary but known incidence angle, 2) be able to measure all reflection angles over the entire 2π of solid angle, and 3) restrict the reflection to be from a single point on this surface (and thus eliminate secondary light collected from multiple reflections inside of the crystal). The second requirement suggests that refractions should be avoided, if possible, in the setup. Many scintillators are high index materials, and as such, are susceptible to total internal reflection, making measurement at that angle impossible.

A schematic of our measurement setup is displayed in Fig. 1. A laser beam is aimed towards the center of a 50.8-mm diameter scintillating crystal hemisphere. The beam enters the crystal perpendicular to the crystal surface, gets reflected off the crystal back surface, and exits the crystal perpendicular to the crystal surface before being recorded by the surrounding array of photodiodes. All light entering and exiting the crystal is perpendicular to the curved surface, eliminating any refraction of the beam, and especially any total internal reflections, making all angles measurable.

All the photodiodes are mounted at a constant radius from the reflection point, exposing each photodiode to equal solid angles.

The instrument design is shown in Fig. 2. The laser can be rotated from theta equal to -90º to +90º. The photodiode array can be independently rotated from theta equal to -90º to +90º, covering 2π of solid angle.
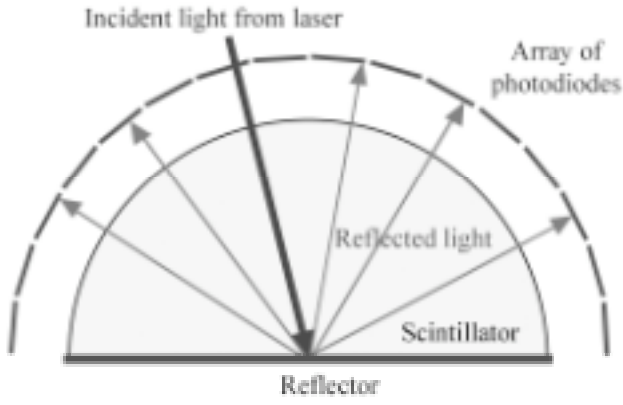
Fig. 1. Schematic of our measurement setup. A laser beam is aimed towards the center of a hemispherical crystal. The angular light reflectance distribution is measured with an array of photodiodes. The figure is not to scale.
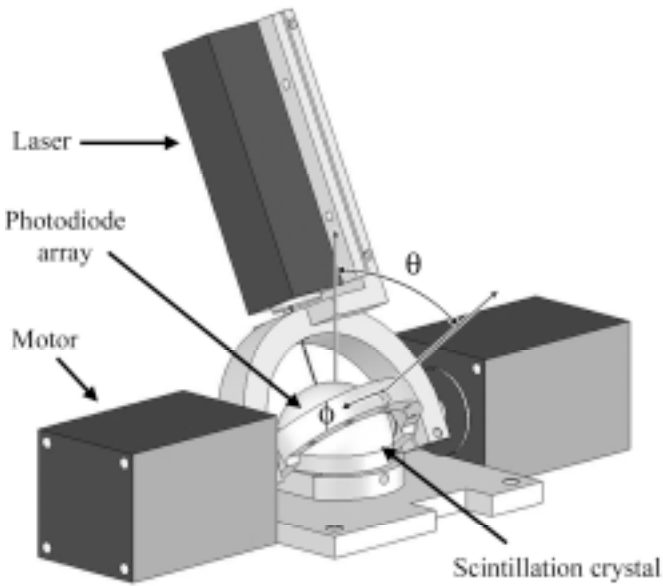

Fig. 2. Scale drawing of the instrument for measuring the light distribution. A laser, mounted on an arch, is aimed towards the center of a hemispherical crystal. The laser can, with a stepper motor, be rotated from theta = -90° to +90°. The photodiode array is mounted on a second arch, and can be rotated from theta = -90° to +90° with a second stepper motor. The theta and phi angles, defined in Fig. 3, display the coordinates for the detectors, which are mounted on the detector arch. The inner radius of the detector arch is 30 mm, and the inner radius of the laser arch is 45 mm. The entire set-up can fit inside of a 380 x 370 x 220 mm^3 box (width x depth x height), with full rotational freedom for the laser.

B. Sampling

The angular sampling of the light reflectance is determined by the photodiode spacing in the phi-angle dimension and by the photodiode arch motion in the theta-angle dimension. This relationship is shown in Fig. 3, including the definitions of the two angles.

When both the laser and the photodiode array are at the same value of theta, the photodiode array will block the incident laser beam. This implies that some region in the theta-phi plane will be un-sampled. Eliminating unnecessary material from the detector arch minimizes this region; however, we cannot fully eliminate this blockage of the laser beam and will have to interpolate the data over this small un-
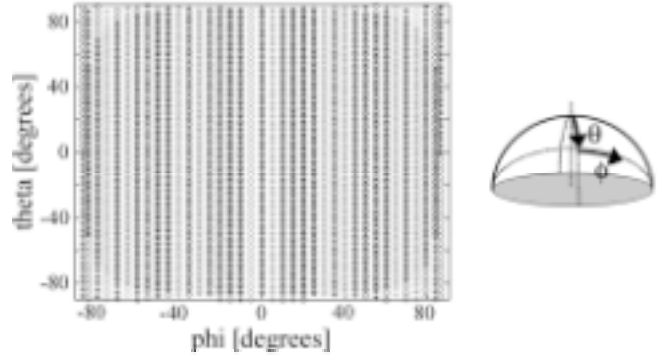
sampled area.

Fig. 3. Angular sampling of the reflectance distribution. The theta sampling is set by the motion of the photodiode array arch (here set to 4° step-size). The phi sampling is set by the photodiode spacing. The figure on the right defines the theta and phi angles. Theta is in the same plane as defined by the motion of the laser beam's incidence angle, also shown in Fig. 2, while phi is along the photodiode arch direction. Each '*' in the left graph represents a photodiode location in theta and phi, and using the symmetry in our setup, we can double the measurement points in phi, represented by the 'o's.

C. Error Analysis

An error analysis was performed to evaluate how a misalignment in our setup translates throughout the system to our measurements when the various parts of our setup are not perfectly aligned. The analysis is divided into two parts, an incident ray error analysis and an outgoing ray error analysis. The incident ray error is defined as the misalignment of the beam spot location from the center of the hemisphere's flat surface. This misalignment occurs when the hemisphere or the beam is misaligned. However, since shifting the beam is equivalent to shifting the hemisphere, we assume our beam is static and only address a hemisphere shift in our analysis.

The outgoing ray error is the angle error defined as the difference between the angle we think we are measuring (beam spot being at the center of the hemisphere back surface) and the angle we are actually measuring (due to the incorrectly positioned beam spot created by the incident ray error), see Fig. 5, i.e. $\alpha_{error} = \alpha - \alpha^*$.
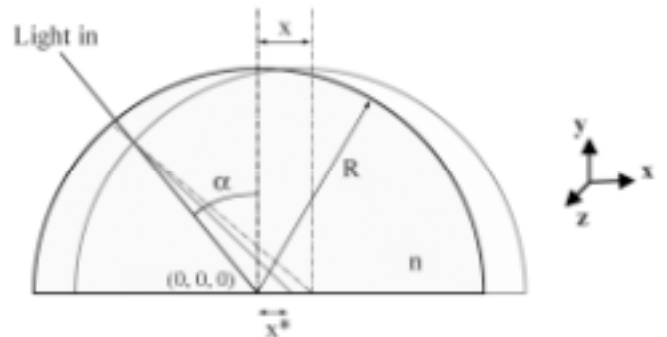

Fig. 4. Misalignment of the hemisphere in the x-direction. A shift of the hemisphere by x in the x-direction causes an x* misalignment of the beam spot relative to the center of the hemisphere.

$$x^* = \cfrac{x}{n\left(\sqrt{1-\left(\dfrac{x\cos(\alpha)}{R}\right)^2}\sqrt{1-\left(\dfrac{x\cos(\alpha)}{nR}\right)^2} - \dfrac{x\sin(\alpha)}{R\sqrt{1-\left(\dfrac{x\cos(\alpha)}{nR}\right)^2}} + \dfrac{x\sin(\alpha)}{nR\sqrt{1-\left(\dfrac{x\cos(\alpha)}{R}\right)^2}} + \dfrac{x^2\cos^2(\alpha)}{nR^2}\right)} \tag{1}$$

$$x^*_{\pm} = \cfrac{y\sin(\alpha)}{n\left(\cos(\alpha)\sqrt{1-\left(\dfrac{y\sin(\alpha)}{R}\right)^2}\sqrt{1-\left(\dfrac{y\sin(\alpha)}{nR}\right)^2} + \dfrac{y\sin^2(\alpha)}{R}\left(\dfrac{y\cos(\alpha)}{nR}\pm\dfrac{\sqrt{1-\left(\dfrac{y\sin(\alpha)}{R}\right)^2}}{n}\mp\sqrt{1-\left(\dfrac{y\sin(\alpha)}{R}\right)^2}\right)\right)} \tag{2}$$

$$z^* = \cfrac{1}{\left(\dfrac{z}{R^2}+\sqrt{\dfrac{n^2}{z^2}+\dfrac{1+n^2}{R^2}+\dfrac{z^2}{R^4}}\right)} \tag{3a} \qquad \Longrightarrow \qquad z^* \xrightarrow[z\ll R]{} \frac{z}{n} \tag{3b}$$

$$\sin(\alpha_{error}) = \frac{nx^*\cos(\alpha^*)}{R+\Delta}\sqrt{1-\left(\frac{nx^*\cos(\alpha^*)}{R}\sqrt{1-\left(\frac{x^*\cos(\alpha^*)}{R}\right)^2}-\frac{x^*\cos(\alpha^*)}{R}\sqrt{1-n^2\left(\frac{x^*\cos(\alpha^*)}{R}\right)^2}\right)^2}+$$
$$-\left(\frac{nx^*\cos(\alpha^*)}{R}\sqrt{1-\left(\frac{x^*\cos(\alpha^*)}{R}\right)^2}-\frac{x^*\cos(\alpha^*)}{R}\sqrt{1-n^2\left(\frac{x^*\cos(\alpha^*)}{R}\right)^2}\right)\sqrt{1-\left(\frac{nx^*\cos(\alpha^*)}{R+\Delta}\right)^2} \tag{4}$$
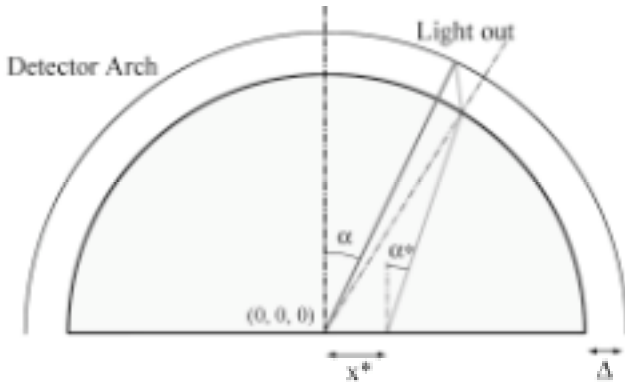

Fig. 5. Outgoing ray error. An x* misalignment of the beam spot causes the incorrect angle α* to be measured.

The incident ray error is divided into three separate cases; horizontal x and z shifts, and a vertical y shift, respectively. The horizontal x shift leading to an x* misalignment for the beam spot on the hemisphere back surface is demonstrated in Fig. 4. The y and z misalignments can be shown in similar fashion. Note that for a vertical shift in y, the incident ray error will occur in the horizontal plane, in x. The coordinate system we are using is the Cartesian, with x and z lying in the flat surface plane and y being perpendicular to this plane, as shown on the right in Fig. 4.

A shift of the hemisphere in x will result in a beam spot position of x* according to (1). Similarly, a shift in y will result in x*, see (2), and a shift in z will result in a beam spot position of z*, see (3a). The error in the z-direction can be approximated by (3b) for small shifts in z.

For the equations: n is the index of refraction for the scintillating crystal, R is the hemisphere radius, α is the incidence angle, and x is the shift in the x-direction. Similarly, y and z are shifts in the y- and z-directions. The outgoing ray error is calculated in (4). All equations were derived from simple geometry and trigonometry.

Using these equations for BGO, with $n = 2.1$, 25.4-mm radius hemisphere, a horizontal shift of 0.5 mm, and a vertical shift of 0.25 mm, we get an error that is less than 1° for any outgoing ray angle for all incidence angles less than 80°. This should be compared to a photodiode coverage of 6.3° x 3.8°, as described in the *III.B Light Detection* section.

D. Beam size

A finite beam width is equivalent to a translation of the incident beam, which was analyzed in the previous section. Using those results, beam widths less than 1 mm imply angular errors of less than 1°. In addition, the hemispherical shape of the scintillator acts as focusing lens, so that the diameter of the beam at the studied reflection surface is a factor n smaller than the incident beam diameter, where n is the index of refraction. This reduction in size is beneficial, as

it reduces the area that is illuminated when the beam is incident at an oblique angle.

III. COMPONENT SELECTION

A. Light Source

For measurements to be performed over an extended period of time, the light source has to be very stable in output power, or alternatively, the output power has to be continuously monitored to be able to correct for the variations. Furthermore, the light source should not be too powerful (for safety reasons), un-polarized (the light emitted from a scintillating crystal is generally assumed to be un-polarized [1], however, this seems to be dependent on the crystal material), the wavelength should lie between 390 nm and 480 nm (where most common scintillators have their peak emission [9]), and the light source should be rotation insensitive. Besides these critical requirements, we also wanted the light source to fit in a small package that does not require alignment or adjustment, as well as that the light source is energy efficient so it does not heat up the other electronic components in the black box it will be placed in.

We found these requirements fulfilled by a 440 nm solid-state laser offered by CrystaLaser® [Reno, NV]. To verify that the laser fulfills our requirements, as well as meets the manufacturer's specifications, several tests were performed.

The laser manufacturer specified the power stability to be 0.8% over 24 hours. We tested the laser's power output stability over time by irradiating a photodiode over 48 hours while recording the produced current. During this test, the air temperature was monitored in the black box which contained the setup. The acquired data are displayed in Fig. 6 and Fig. 7. A strong anti-correlation was observed between the laser output power and the air temperature, so we applied a linear temperature correction of -0.56% / ºC to the current data, and display the results in Fig. 8. (The correction coefficient was calculated from an independent acquisition.) With the temperature correction, the power instability was measured to be <±0.25% over 48 hours. If the temperature correction is not applied, the instability was measured to be <±1.5% over 48 hours, see Fig. 6.

The manufacturer specified the beam size to be a TEM_{00} beam with <0.9 mm diameter. The beam profile was measured by stepping the laser past a photodiode with a 0.3 mm wide slit in front of the diode. The un-collimated beam was measured to be 0.56 mm full-width-at-half-maximum (FWHM) in the vertical direction and 1.12 mm FWHM in the horizontal direction. To decrease the horizontal beam profile width, we glued a 1-mm diameter pinhole to the front of the laser. This decreased the horizontal beam width to 0.72 mm FWHM. The vertical beam profile remained unchanged. The collimated horizontal and vertical beam profiles are displayed in Fig. 9 and do not show any measurable diffraction effects from the collimator. The collimation also lowered the maximum output power of the laser from 7.0 mW to 4.3 mW, converting the laser into a Class IIIa type laser.

The power output was also measured with the laser beam passing through a polarization filter. The output was measured to be constant within <±4.6% over all polarization angles.

The beam width was measured at various distances to the laser. The beam divergence angle was measured to be -0.026º (beam converging) for distances from the laser of 1 cm to 20 cm. This beam divergence is not significant for the distances the laser will be used at.

TABLE I
LASER CHARACTERISTICS (MEASURED)

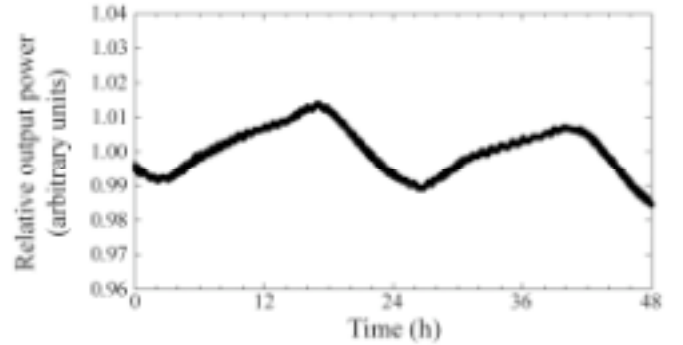|		
Wavelength	440 nm	
Power Stability, Uncorrected	< ±1.5% over 48 hours	
Power Stability, Corrected	< ±0.25% over 48 hours	
Beam Divergence	-0.026º (beam converging)	
Polarization Power	<±4.6% over 360º	
	Before collimation	After collimation
Horizontal Beam Size	1.12 mm FWHM	0.72 mm FWHM
Vertical Beam Size	0.56 mm FWHM	0.56 mm FWHM
Output Power	7.0 mW	4.3 mW
Laser Class	III b	III a

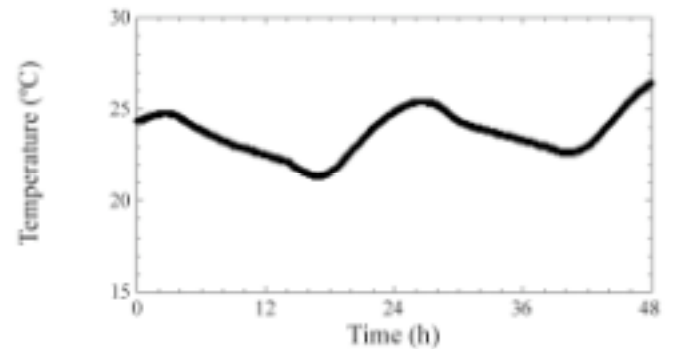Fig. 6. Measured output power of the laser as a function of time.

Fig. 7. Measured air temperature in the black box as a function of time. The temperature was measured while recording the laser output power displayed in Fig. 6.
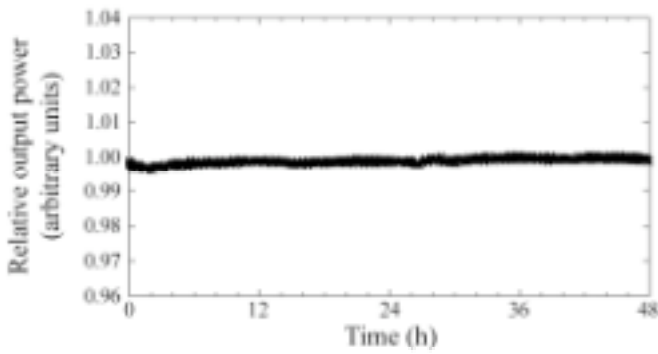
Fig. 8. Temperature-corrected output power of the laser. A linear temperature correction for the data from Fig. 6 was used with -0.56% per °C. The correction coefficient was calculated from an independent acquisition.
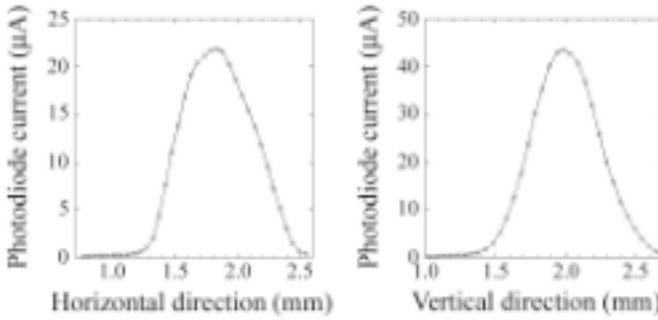

Fig. 9. Profiles of the collimated laser beam in the horizontal (left) and vertical (right) directions, respectively. A 0.3 mm slit was used when measuring the profiles. The horizontal FWHM was measured to be 0.72 mm and the vertical FWHM was measured to be 0.56 mm.

Rotating the laser around its axes in the horizontal planes as well as the vertical plane had no effect on the output power.

The tests verified that the laser meets all of our specifications, and the laser stability can be further improved if a temperature correction is applied.

B. Light Detection

We chose Hamamatsu [Japan] S8729 PIN photodiodes as our light detectors. We chose to use single photodiode detectors even though a linear array would achieve a higher spatial resolution. A linear array would not fit as easily between the laser arch and the hemisphere, and it would require corrections for the varying solid angles along the curvature of the detector arch. Further requirements we had on the photodiodes were that they have to have a high active-to-dead area ratio, a small physical size, and good quantum efficiency. The physical size of the S8729 is 5 mm x 4 mm, with the active area being 3.3 mm x 2 mm. The quantum efficiency for the S8729 is 63% at 440 nm, which corresponds to 0.23 A/W.

All photodiodes were tested for quantum efficiency uniformity by illuminating them with the laser beam. The photodiodes were operated in photovoltaic mode. We measured all photodiode currents to be 0.23 A/W ± 1%, see Fig. 11. The dark current was measured to be less than 10 nA.

To be able to fit all photodiodes within the small amount of space that exists between the crystal hemisphere and the laser arch, a rigid-flex printed circuit board (PCB) was designed. Eighteen photodiodes are mounted on each rigid-board, which is shaped as an arch. A flexible Kapton cable connects the arch with a 26-pin connector socket on a second rigid-board. This second board also contains RC circuits for noise reduction.
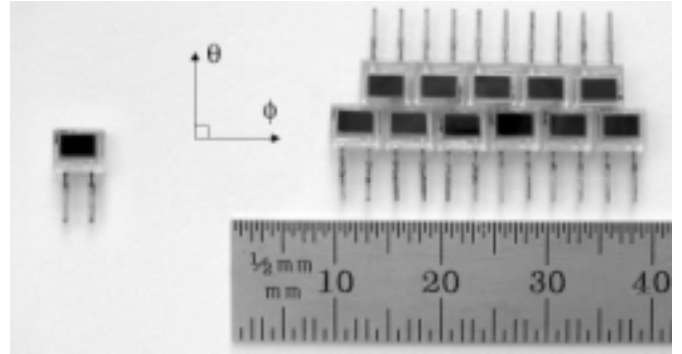

Fig. 10. Hamamatsu's S8729 pin photodiodes. The physical size for each photodiode is 5 mm x 4 mm, and the active area is 3.3 mm x 2 mm. The theta-phi coordinate system, defined in Fig. 3, has been added to the photograph to clarify the photodiode orientations when mounted on the detector arch.

Each photodiode's active area covers 6.3° (in phi) x 3.8° (in theta). The photodiodes are mounted on the PCB in such a way that the first PCB holds a row of 18 photodiodes. The second row of photodiodes, on the second PCB and also containing 18 photodiodes, is offset to the first by half a detector length, as illustrated in Fig. 10. This arrangement allows us to achieve 5 degree sampling in the phi direction.
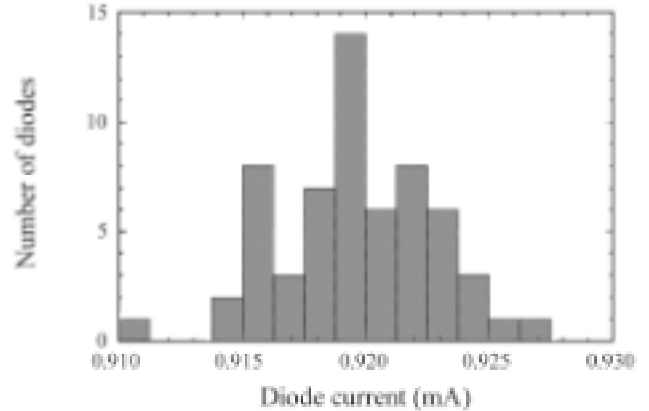

Fig. 11. Current response for 60 photodiodes. The irradiating laser power was set to 3.9 mW and the produced current was averaged over 10 s.

There is a trade-off between the angular resolution of the proposed setup and the dynamic range (described in the *III.C Electronics* section) of the photodiodes. By increasing the distance between the photodiode array and the surface we want to examine, we increase the angular resolution but also increase the angular error (see the *II.C Error Analysis* section) for a misaligned hemisphere. The signal-to-noise ratio also decreases as less light is detected by each photodiode. We expect most variations in the angular light distribution to be slowly varying, so we mounted the photodiodes at a radius of 30 mm, which gives ~5° angular sampling and <1° angular error.

C. Electronics

The currents from the photodiodes are switched through a

National Instruments Corporation [Austin, TX] PXI-2503 48-channel multiplexer to a National Instruments PXI-4070 6_ digit digital multimeter (DMM). The DMM has a 10 nA resolution in the 20 mA current setting. Since the largest current produced with our laser should be about one mA, we achieve a dynamic current range of $10^5:1$.

A LabVIEW program controls the multiplexer, the DMM, and the data handling.

To fully sample 2π of solid angle we need to make, not using any symmetry assumptions, ~1100 photodiode readouts. This is less than the 46 x 36 measurements (theta-steps times number of photodiodes) shown in Fig. 3, as there is over-sampling at large phi angles. Performing an acquisition with 3 seconds averaging for the photodiode current readout, sampling every 4° for the laser incidence angle, and taking into account the time delays for the motion of the arches, we expect an acquisition time of about 24 hours per scintillator sample.

D. Motion Control

The motion of the laser arch and the detector arch are controlled by NEMA 23 sized stepper motors and gear heads. The gear heads are planetary gear heads to minimize the backlash, which is below 10 arc minutes. The gear ratio is 22:1, and the stepper motors torque is well within the requirements for our setup. Although the minimum angular increment for the stepper motors and gear heads is 0.04°, the angular accuracy is limited by the backlash of the gear heads. To minimize the error in the angular positioning we will 1) home the arches before each new measurement, 2) always step in the same direction when acquiring data, and 3) use absolute coordinates for the stepper motors to eliminate any accumulative errors in the advancement of the arches. The LabVIEW program mentioned under the *III.C Electronics* section also controls the motion of the stepper motors.

E. Glove Box

The entire setup is housed in a Terra Universal, Inc., [Fullerton, CA] series 100 glove box custom made with black acrylic. The glove box measures 890 x 610 x 560 mm^3 (width x depth x height), large enough to hold the entire instrument yet small enough to be placed on a workbench. The viewing windows are made in clear acrylic to allow us to monitor our setup. The reason for using a glove box is to be able to control the water content in the air. By flowing dry nitrogen through the box, we can control the water content in the air down to 1 ppm, thus enabling us to measure hygroscopic materials.

F. Scintillation Samples

Our instrument is designed to be able to measure scintillator hemispheres with up to 50.8-mm diameters. However, the setup allows us also to measure smaller hemispheres, which is important when we want to characterize scintillators that are not available in the 50.8-mm diameter size.

We have been able to acquire hemispherical shaped scintillators from several suppliers of scintillators. We have also contracted an optical company to polish samples of scintillators to hemispheres. To make sure we have round hemispheres, the roundness of each hemisphere sample will be measured. We will use a Carl Zeiss Industrial Metrology [Germany] Accura® 16-30-14 MPS scanning probe for these measurements. This active scanning probe will allow us to measure how the crystal hemispheres deviate from a perfect hemispherical shape. The Accura® has a maximum error of 3.7 μm for 50.8-mm diameter hemispheres. A preliminary measurement on a plastic hemispherical scintillator with a 50.8-mm diameter resulted in less than 4 μm local (over 2°) surface variations, and less than 10 μm global (over 360°) surface variations. This measurement translates into local angle variations that are less than 0.3°.

IV. CONCLUSIONS

We have designed an instrument to measure the light reflectance distribution within a scintillating crystal as a function of incidence angle, material, surface, and reflector characteristics. The angular reflection distribution with this instrument can be measured with 1% accuracy. This will aid in: 1) characterizing scintillating crystals and 2) creating more accurate models for light reflection distribution within scintillating crystals.

Based on the encouraging results presented in this paper, we have started to construct the proposed instrument.

REFERENCES

[1] A.P. Dhanasopon, C.S. Levin, A.M.K. Foudray, P.D. Olcott, and F. Habte, "Scintillation Crystal Design Features for a Miniature Gamma Ray Camera", *IEEE Trans. Nucl. Sci.*, vol. 52, no. 5, pp. 1439-1446, Oct 2005.

[2] D. Nikolopoulosa, I. Valaisa,b, I. Kandarakisa, D. Cavourasa, D. Linardatosa, I. Sianoudisc, A. Louizid, N. Dimitropoulose, D. Vattisc, A. Episkopakisa, C. Nomicosf, and G. Panayiotakisb, "Evaluation of the GSO:Ce scintillator in the X-ray energy range from 40 to 140 kV for possible applications in medical X-ray imaging", *Nucl. Instr. and Meth. A*, vol. 560, pp. 577–583, 2006.

[3] T.T. Monajemi, S. Steciw, B.G. Fallone, and S. Rathee, "Modeling scintillator-photodiodes as detectors for megavoltage CT", *Medical Physics*, vol. 31, no. 5, pp. 1225-1234, May 2004.

[4] H. Rothfuss, M. Casey, M. Conti, N. Doshi, L. Eriksson, and M. Schmand, "Monte Carlo Simulation Study of LSO Crystals", *IEEE Trans. Nucl. Sci.*, vol. 51, no. 3, pp. 770-774, June 2004.

[5] F. Cayouette, C. Moisan, N. Zhang, and C.J. Thompson, "Monte Carlo Modeling of Scintillator Crystal Performance for Stratified PET

Detectors With DETECT2000", *IEEE Trans. Nucl. Sci.,* vol. 49, no. 3, June 2002.

[6] G.F. Knoll, T.F. Knoll, and T.M. Henderson, "Light collection in scintillating detector composites for neutron detection," *IEEE Trans. Nucl. Sci.*, pt. 1, vol. 35, pp. 872–875, Feb. 1988.

[7] F. Cayouette, D. Laurendeau, and C. Moisan, "DETECT2000: An Improved Monte-Carlo Simulator for the Computer Aided Design of Photon Sensing Devices", *Proc. SPIE Photonic North*, Quebec, Canada, June 2002

[8] F.-X. Gentit, "Litrani: a general purpose Monte-Carlo program simulating light propagation in isotropic or anisotropic media", *Nucl. Instr. and Meth. A*, vol. 486, no. 1-2, pp., p. 35, June 2002

[9] C.L. Melcher, "Scintillation crystals for PET", *J. Nucl. Med.*, vol. 41, no. 6, pp. 1051-1055, June 2000.